Protein Cell 2022, 13(9):676–682
https://doi.org/10.1007/s13238-021-00898-9

Protein & Cell

LETTER

mTORC2/RICTOR exerts differential levels of metabolic control in human embryonic, mesenchymal and neural stem cells

Dear Editor,

Stem cells, including pluripotent stem cells and adult stem cells, possess the remarkable capability of being able to self-renew while at the same time having potential to differentiate into different cell lineages and functionally distinct cell types. Human embryonic stem cells (hESCs) can differentiate into all adult stem cell types, including human mesenchymal stem cells (hMSCs) and human neural stem cells (hNSCs), but can also give rise to all terminally differentiated cell types (Wang et al., 2021a). Through the continuous replenishment of differentiated cells, stem cells support tissue homeostasis and respond to tissue injuries. Given the promising applications of stem cells in cell therapy and regenerative medicine, insights into molecular events underlying stem cell maintenance, self-renewal ability and pluripotency, continue to garner strong interest (Shan et al., 2021). Although metabolic pathways have been implicated in the reciprocal regulations of stem cell self-renewal and differentiation as well as organ homeostatic maintenance (Garcia-Prat et al., 2017), central aspects of how metabolic requirements differ and are regulated across the various types of human stem cells in our body remain enigmatic.

The mammalian target of rapamycin (mTOR) pathway is one of the most important metabolic pathways in mammals, and accordingly, it is pivotal for multiple cellular activities in stem cells (Meng et al., 2018). The mTOR pathway comprises two distinct protein complexes, complex 1 (mTORC1) with associated regulatory protein RAPTOR, and complex 2 (mTORC2) with the rapamycin-insensitive companion RICTOR, as respective core unique components. Given that numerous clinical trials have been funded to investigate the safety and efficacy of mTOR inhibitors, it is of both scientific and clinical importance to gain a deeper knowledge about the role of mTOR pathway, and especially for the lesser known mTORC2, in the homeostatic maintenance of different types of human stem cells.

To investigate whether and how RICTOR may regulate human stem cells, we used CRISPR/Cas9-mediated gene editing in hESCs to introduce indels in exon 1 of the *RICTOR* gene (Fig. 1A and 1B). This approach successfully knocked out RICTOR as validated by western blot analysis showing the ablation of RICTOR protein. Alongside, S473 phosphorylation of AKT, which is a major substrate of mTORC2 (Wang et al., 2021b), was also downregulated in $RICTOR^{-/-}$ hESCs (Figs. 1C and S1A). RICTOR-deficient hESCs were karyotypically normal (Fig. S1B) and maintained genomic integrity, as exemplified by genome-wide copy number variation (CNV) analysis (Fig. S1C). However, RICTOR deficiency caused aberrant colony morphology (Fig. 1D), shown as a marginal differentiation of the clone, a phenotype frequently observed in hESCs with compromised pluripotency. Concomitantly, the expression of stem cell pluripotency markers OCT4, SOX2 and NANOG, along with others, were downregulated (Figs. 1E, S1D and S1E). Disrupted alkaline phosphatase staining and attenuated capability for teratoma formation further confirmed the impaired pluripotency of $RICTOR^{-/-}$ hESCs (Fig. 1F–1H). Additionally, RICTOR deficiency attenuated clonal expansion ability and disrupted hESC cell cycle kinetics (Figs. 1I and S1F). Altogether, these observations suggest that RICTOR deficiency attenuates hESC self-renewal and pluripotency.

Next, we differentiated $RICTOR^{+/+}$ and $RICTOR^{-/-}$ hESCs into hMSCs and hNSCs to assess how RICTOR loss-of-function (LOF) impacts on human adult stem cells (Fig. 1A). As expected, RICTOR protein was depleted in $RICTOR^{-/-}$ hMSCs along with decreased AKT S473 phosphorylation (Fig. S1G and S1H). Yet, $RICTOR^{-/-}$ hMSCs maintained genomic integrity as demonstrated by CNV analysis (Fig. S1I) and normal cellular morphology along with the expression of hMSC-specific markers including CD73, CD90 and CD105 as previously described (Bi et al., 2020) (Figs. 1J and S1J). By contrast, RICTOR deficiency led to decreased self-renewal ability in hMSCs, as evidenced by lower clonal expansion ability, fewer Ki67 positive cells (Fig. 1K and 1L). RICTOR deficiency also impeded the differentiation potentials of hMSCs into osteoblasts, chondrocytes and adipocytes (Figs. 1M and S1K). As for $RICTOR^{-/-}$ hNSCs, RICTOR protein was completely absent together with decreased AKT S473 phosphorylation (Fig. S1L and S1M). Likewise, $RICTOR^{-/-}$ hNSCs expressed hNSC-specific markers PAX6 and SOX2 (Figs. 1N and S1N) as

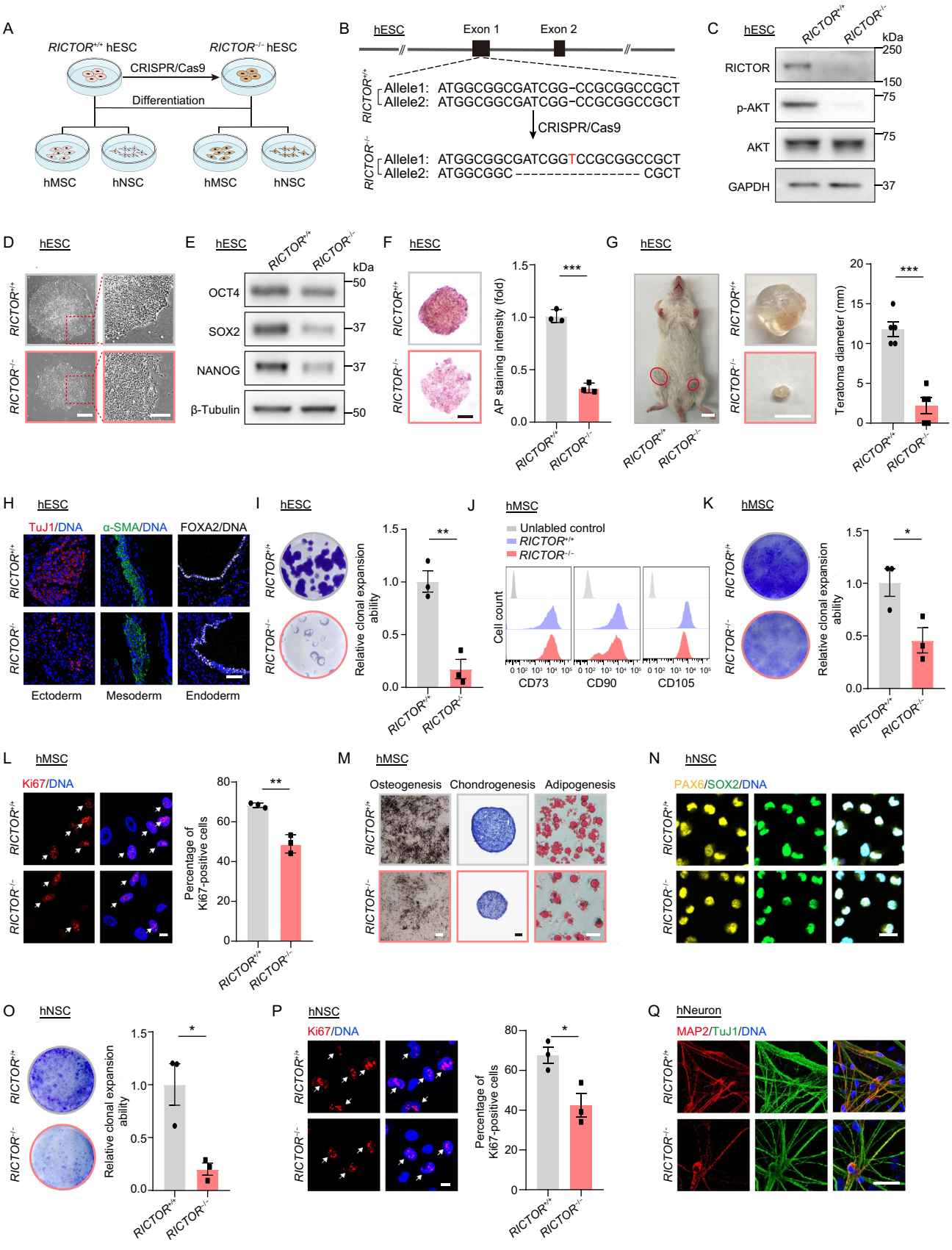

Protein & Cell

Figure 1. RICTOR deficiency attenuates pluripotency and differentiation abilities of hESCs, hMSCs and hNSCs. (A) Schematic diagram of the generation of RICTOR-deficient hESCs and hESC-derived hMSCs and hNSCs. (B) Schematic of the deletion of *RICTOR* via CRISPR/Cas9-mediated non-homologous end-joining (NHEJ). The diagram shows the first 2 out of 38 exons of *RICTOR* along with the edited sequence in exon 1. (C) Western blot analysis of RICTOR, phosphorylated AKT Ser473 and total AKT expression in $RICTOR^{+/+}$ and $RICTOR^{-/-}$ hESCs. GAPDH was used as the loading control. (D) Representative phase-contrast images of $RICTOR^{+/+}$ and $RICTOR^{-/-}$ hESC colonies. Scale bar, 200 μm and 100 μm (zoomed-in image). (E) Western blot analysis of the pluripotency markers OCT4, SOX2 and NANOG expression in $RICTOR^{+/+}$ and $RICTOR^{-/-}$ hESCs. β-Tubulin was used as the loading control. (F) Representative alkaline phosphatase staining of hESCs. Scale bar, 200 μm. Data are representative of three biological repeats. ***$P < 0.001$. (G) Average diameters of teratomas formed by $RICTOR^{+/+}$ and $RICTOR^{-/-}$ hESCs. Scale bar, 10 mm. Data are presented as mean ± SEM of five biological repeats. ***$P < 0.001$. (H) Immunofluorescence staining of the differentiation markers for three germ layers in teratoma, Scale bar, 50 μm. (I) Clonal expansion analysis of $RICTOR^{+/+}$ and $RICTOR^{-/-}$ hESCs. Data are presented as mean ± SEM of three independent experiments. **$P < 0.01$. (J) Flow cytometry analysis of hMSC-specific surface markers CD73, CD90 and CD105 in $RICTOR^{+/+}$ and $RICTOR^{-/-}$ hMSCs (passage 3). (K) Clonal expansion analysis of $RICTOR^{+/+}$ and $RICTOR^{-/-}$ hMSCs (passage 4). Data are presented as mean ± SEM of three independent experiments. *$P < 0.05$. (L) Immunofluorescence analysis of Ki67 expression in $RICTOR^{+/+}$ and $RICTOR^{-/-}$ hMSCs (passage 4). Scale bar, 10 μm. Data are presented as mean ± SEM of three biological repeats. **$P < 0.01$. (M) Characterization of the multilineage differentiation potentials of hMSCs (passage 4). Left, osteogenesis of $RICTOR^{+/+}$ and $RICTOR^{-/-}$ hMSCs evaluated by von Kossa staining. Scale bar, 250 μm. Middle, chondrogenesis of $RICTOR^{+/+}$ and $RICTOR^{-/-}$ hMSCs evaluated by Toluidine blue staining. Scale bar, 50 μm. Right, adipogenesis of $RICTOR^{+/+}$ and $RICTOR^{-/-}$ hMSCs evaluated by Oil Red O staining. Scale bar, 50 μm. (N) Immunofluorescence staining for hNSC-specific markers PAX6 and SOX2 in $RICTOR^{+/+}$ and $RICTOR^{-/-}$ of hNSCs (passage 3). Scale bar, 20 μm. (O) Clonal expansion analysis of $RICTOR^{+/+}$ and $RICTOR^{-/-}$ hNSCs (passage 5). Data are presented as mean ± SEM of three independent experiments. *$P < 0.05$. (P) Immunofluorescence analysis of Ki67 expression in $RICTOR^{+/+}$ and $RICTOR^{-/-}$ hNSCs (passage 5). Scale bar, 10 μm. Data are presented as mean ± SEM of three biological repeats. *$P < 0.05$. (Q) Immunofluorescence staining of hNeuron-specific markers MAP2 and TuJ1 in $RICTOR^{+/+}$ and $RICTOR^{-/-}$ hNeurons. Scale bar, 50 μm.

previously described (Wang et al., 2020) and maintained genomic integrity, as shown by CNV analysis (Fig. S1O). In line with our findings in hMSCs, RICTOR deficiency led to decreased proliferative ability (Fig. 1O and 1P) and impaired neuronal differentiation in hNSCs, as reflected by lower percentage of cells positive for neuron-specific markers MAP2 (Figs. 1Q and S1P). Altogether, these results indicate that RICTOR deficiency impairs self-renewal and differentiation of hMSCs and hNSCs.

To elucidate molecular mechanisms underlying RICTOR LOF and how these contribute to compromised hESC self-renewal and differentiation capabilities, we carried out genome-wide RNA sequencing (RNA-seq) analysis. In total, we identified 585 upregulated genes and 530 downregulated genes in $RICTOR^{-/-}$ hESCs (Fig. S2A and S2B). Pathway and gene ontology (GO) enrichment analysis revealed that the upregulated genes were mainly associated with oxidative phosphorylation (exemplified by genes such as *ATP5MC3*, *ATP5MF*) and mitochondrial organization (*FIS1*, *TOMM7*), and that the downregulated genes were related to extracellular structure organization (*COL1A2*, *COL5A2*) and stemness maintenance (*KIT*, *ZIC3*) (Fig. 2A). These findings likely pinpoint mitochondrial modulation as the core mechanism causing dysregulation of hESC homeostasis upon RICTOR deficiency. Given that glycolysis regulates hESC self-renewal (Gu et al., 2016), we examined the changes in glycolysis in hESCs with RICTOR deficiency. Consistent with the aforementioned impaired hESC self-renewal upon RICTOR ablation, we observed decreased glycolysis in $RICTOR^{-/-}$ hESCs (Fig. 2B). Subsequently, we evaluated the changes in the mitochondria between $RICTOR^{+/+}$ and $RICTOR^{-/-}$ hESCs and detected increases in mitochondrial number per cell and relative mitochondrial mass, suggesting higher mitochondrial content associated with RICTOR deficiency (Figs. 2C, 2D and S2C). By contrast, the ablation of RICTOR in hESCs caused disarranged cristae structure (Fig. 2C), increased mitochondrial ROS and decreased mitochondrial membrane potential (Fig. S2D and S2E), indicative of impaired mitochondrial fitness. Overall, although baseline mitochondrial respiration was comparable between $RICTOR^{+/+}$ and $RICTOR^{-/-}$ hESCs, the maximal respiratory ability was higher in $RICTOR^{-/-}$ hESCs likely due to increased mitochondrial content (Fig. 2E). Altogether, these data indicate that RICTOR deficiency causes changes in glycolytic capacity and mitochondrial fitness in hESCs, likely contributing to impaired self-renewal capability.

To determine the molecular mechanisms underlying RICTOR deficiency in human embryonic and adult stem cells, we performed RNA-seq analysis of hMSCs and hNSCs derived from $RICTOR^{+/+}$ and $RICTOR^{-/-}$ hESCs. In total, we identified 814 upregulated genes and 1,113 downregulated genes in hMSCs, and 1,056 upregulated genes and 530 downregulated genes in hNSCs (Fig. S2A and S2B). However, when we compared the DEGs identified in hMSCs and hNSCs to those of hESCs, we found that shared genes were relatively few, with only 14 upregulated and 29

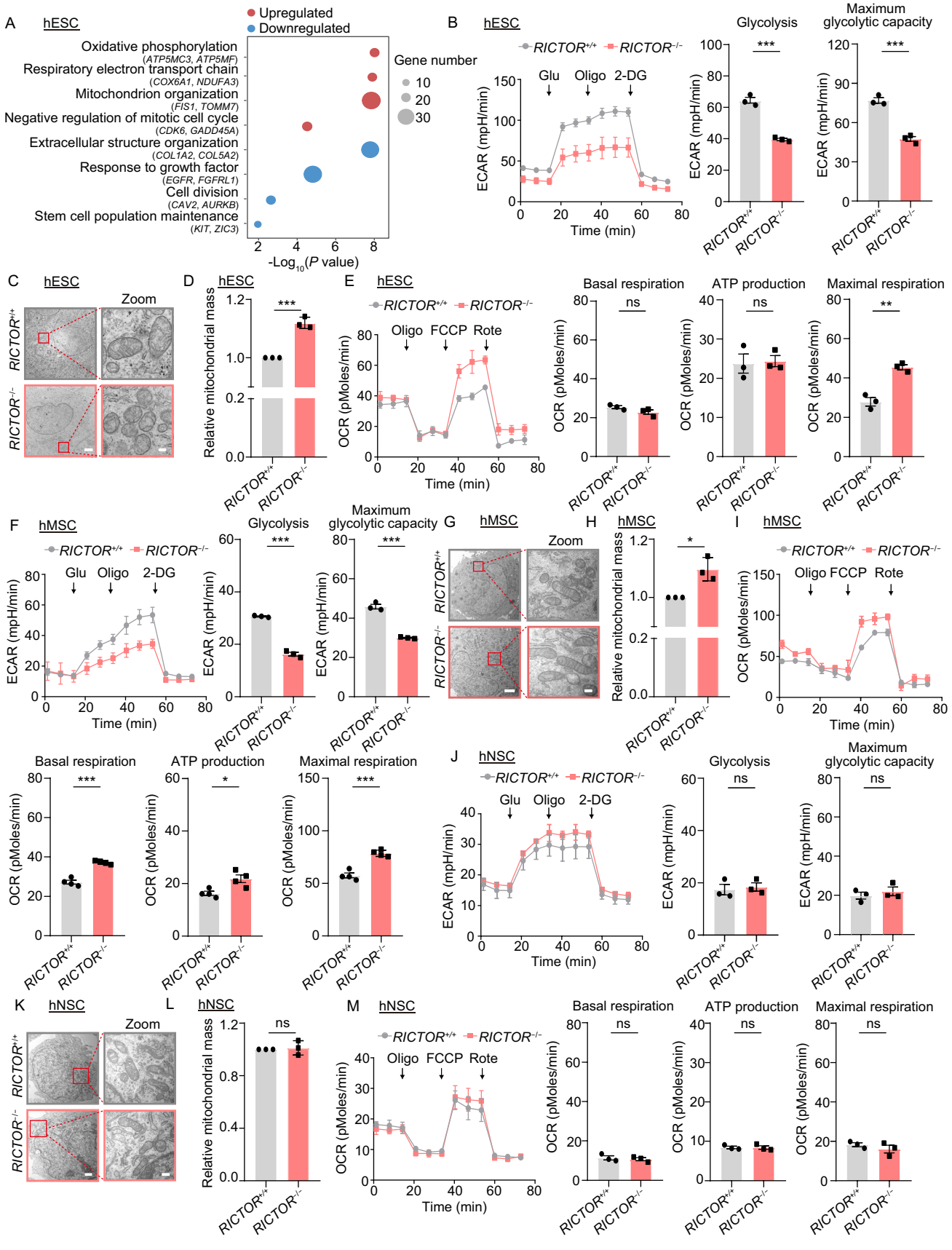

Figure 2. RICTOR deficiency exerts differential effects on mitochondrial fitness in hESCs, hMSCs and hNSCs. (A) GO and pathway enrichment analysis of differentially expressed genes in *RICTOR*$^{+/+}$ and *RICTOR*$^{-/-}$ hESCs. (B) Representative quantifications of extracellular acidification rates (ECAR) of *RICTOR*$^{+/+}$ and *RICTOR*$^{-/-}$ hESCs. Data are presented as mean ± SEM of three biological repeats. ***P < 0.001. (C) Representative transmission electron microscopy images of *RICTOR*$^{+/+}$ and *RICTOR*$^{-/-}$ hESCs. Scale bars, 2 μm and 200 nm (zoomed-in image). (D) Flow cytometric analysis of mitochondrial mass in hESCs. Data are presented as mean ± SEM of three independent experiments. ***P < 0.001. (E) Cellular oxygen consumption rates (OCR) of *RICTOR*$^{+/+}$ and *RICTOR*$^{-/-}$ hESCs in response to indicated mitochondrial modulators. Data are presented as mean ± SEM of three biological repeats. ns, not significant, **P < 0.01. (F) Representative quantifications of extracellular acidification rates (ECAR) of *RICTOR*$^{+/+}$ and *RICTOR*$^{-/-}$ hMSCs (passage 4). Data are presented as mean ± SEM of three biological repeats. ***P < 0.001. (G) Representative transmission electron microscopy images of *RICTOR*$^{+/+}$ and *RICTOR*$^{-/-}$ hMSCs (passage 4). Scale bars, 2 μm and 200 nm (zoomed-in image). (H) Flow cytometric analysis of mitochondrial mass in hMSCs (passage 4). Data are presented as mean ± SEM of three independent experiments. *P < 0.05. (I) Cellular oxygen consumption rates (OCR) of *RICTOR*$^{+/+}$ and *RICTOR*$^{-/-}$ hMSCs (passage 4) in response to indicated mitochondrial modulators. Data are presented as mean ± SEM of four biological repeats. *P < 0.05, ***P < 0.001. (J) Representative quantifications of extracellular acidification rates (ECAR) of *RICTOR*$^{+/+}$ and *RICTOR*$^{-/-}$ hNSCs (passage 5). Data are presented as mean ± SEM of three biological repeats. ns, not significant. (K) Representative transmission electron microscopy images of *RICTOR*$^{+/+}$ and *RICTOR*$^{-/-}$ hNSCs (passage 5). Scale bars, 1 μm and 200 nm (zoomed-in image). (L) Flow cytometric analysis of mitochondrial mass in hNSCs (passage 5). Data are presented as mean ± SEM of three independent experiments. ns, not significant. (M) Cellular oxygen consumption rates (OCR) of *RICTOR*$^{+/+}$ and *RICTOR*$^{-/-}$ hNSCs (passage 5) in response to indicated mitochondrial modulators. Data are presented as mean ± SEM of three biological repeats. ns, not significant.

downregulated genes in common (Fig. S2F). Of these downregulated were *BTF3* and *TOX*, previously reported to be related to stem cell maintenance and differentiation (de Jesus Domingues et al., 2016; Hu et al., 2019). By contrast, none of the overlapping genes were related to mitochondrial metabolism (Fig. S2F–S2H), suggesting that RICTOR deficiency impacts on cell type-specific mitochondrial regulatory mechanisms. Accordingly, we measured the changes in mitochondria and metabolism in RICTOR-deficient hMSCs and hNSCs. We found decreased glycolysis in *RICTOR*$^{-/-}$ hMSCs (Fig. 2F), similarly as seen in *RICTOR*$^{-/-}$ hESCs. Besides, RICTOR deficiency did not cause any detectable changes in mitochondrial cristae structure nor mitochondrial ROS levels between *RICTOR*$^{+/+}$ and *RICTOR*$^{-/-}$ hMSCs, but led to increased mitochondrial mass and membrane potential, likely indicative of enhanced mitochondrial respiratory capacity in *RICTOR*$^{-/-}$ hMSCs (Figs. 2G, 2H, S2I and S2J). Indeed, we found that RICTOR deficiency increased both basal and maximal mitochondrial respiration in hMSCs (Fig. 2I). By comparison, in RICTOR-deficient hNSCs, we found RICTOR deficiency did not affect the glycolytic capacity (Fig. 2J), mitochondrial cristae structure, mitochondrial mass nor mitochondrial ROS production in hNSCs (Figs. 2K, 2L and S2K). In contrast to *RICTOR*$^{-/-}$ hMSCs, we detected RICTOR deficiency led to decreased mitochondrial membrane potential in hNSCs (Fig. S2L). However, both basal and maximal mitochondrial respiration were normal in *RICTOR*$^{-/-}$ hNSCs (Fig. 2M), suggesting that the mitochondrial dysregulation caused by RICTOR deficiency in hNSCs is tolerable. Altogether, our findings indicate that RICTOR is critical to the maintenance of mitochondrial fitness in hMSCs, but less important to mitochondrial function in hNSCs.

Here, for the first time, we systematically compared the effects of RICTOR deficiency in human embryonic stem cells and two adult stem cell types. By generating RICTOR-deficient hESCs and executing directed differentiation of these into hMSCs and hNSCs derivatives, we provided a valuable experimental platform for further studying biological roles of RICTOR in human embryonic and adult stem cell types. Our comprehensive analysis demonstrated that RICTOR deficiency adversely affected both self-renewal and differentiation abilities in all three human stem cell types. In addition, we offered novel insights into distinct mitochondrial and metabolic phenotypes caused by RICTOR deficiency in different human stem cells. Specifically, our data show that RICTOR was essential for glycolytic capacity and mitochondrial homeostatic maintenance in hESCs and hMSCs, but its absence led to tolerable mitochondrial defects without changing cell respiration in hNSCs. Our findings suggest that RICTOR maintains the stemness of hESCs and hMSCs likely associated with altered glycolysis and oxidative phosphorylation, and that mitochondrial respiration is largely independent of RICTOR in hNSCs. Overall, our data provide new knowledge about the differential roles of RICTOR in the homeostatic maintenance and mitochondrial regulation of different types of human stem cells.

Because the dysregulation of the mTOR pathway is a hallmark feature of diseases, including metabolic disorders, neurological disease and cardiovascular disease, mTOR is viewed with interest as a potential therapeutic target. To date, most studies on mTOR pathways has focused on mTORC1 via genetic manipulations or targeted pharmacological inhibitors such as rapamycin (Schreiber et al., 2019). By contrast, much less is known about the cellular consequences by interfering with mTORC2. In mice, depletion of Rictor, the unique core regulatory component of mTORC2,

leads to embryonic growth arrest (Zhu et al., 2019) and impedes cardiac differentiation of embryonic stem cells (Zheng et al., 2017). In this study, we found that RICTOR deficiency impaired hESC self-renewal. In addition, our data revealed that RICTOR deficiency had varied impacts on differentiated derivatives and thus brought clarity to its pivotal roles in human stem cell maintenance and highlighting potential molecular and metabolic vulnerabilities in different human progenitor populations, which help us better understand the possible consequences of RICTOR inactivation in clinical cases.

Mitochondrial metabolism impacts on both the self-renewal and differentiation potentials of embryonic stem cells. Pluripotent stem cells have fewer mitochondria and produce energy mainly through glycolysis whereas differentiated cells rely primarily on oxidative phosphorylation and have increased mitochondrial mass. Additionally, attenuated mitochondrial activity negatively regulates cell proliferation and transcriptional activation of genes involved in early differentiation in both mouse and human ESCs (Mandal et al., 2011). Here, we found that RICTOR deficiency led to increased mitochondrial content and respiration in pluripotent hESCs and multipotent hMSCs, likely contributing to their compromised stem cell maintenance. Yet, in multipotent hNSCs, RICTOR deficiency only induced minimal, functionally tolerable changes in mitochondria, suggesting that impaired proliferation and differentiation capabilities of hNSCs lacking RICTOR are uncoupled from mitochondrial respiratory function. Notably, RICTOR has been implicated in multiple signaling pathways related to mitochondria. For instance, mTORC2-AKT-GSK3β signaling pathway participates in the maintenance of mitochondrial fitness and cellular metabolism (Bantug et al., 2018) and mTORC2-mitochondrial Connexin 43 signaling pathway directly modulates mitochondrial function (Wang et al., 2021b). Therefore, it awaits further investigations of the differential molecular mechanisms by which RICTOR deficiency interrupts mitochondrial homeostasis in hESCs and hMSCs, but not in hNSCs. Overall, our comparative data reveal RICTOR-dependent diverse mitochondria-regulatory and stemness maintenance mechanisms in human stem cell populations, possibly reflecting different metabolic needs in specific cell types or different degrees of pluripotency.

Taken together, our findings provide a molecular and functional basis for understanding how RICTOR regulates cellular and mitochondrial homeostasis in different human stem cells. As such, our data send a cautionary note for considering potential adverse effects resulting from treatment of various diseases using mTOR inhibitors, and offer important hints for the prognosis and even prevention of possible cellular and mitochondrial consequences in human stem cells in therapeutic strategies targeting RICTOR or other components of the mTOR pathway.

FOOTNOTES

We are grateful to Lei Bai, Luyang Tian, Ruijun Bai, Jing Lu, Ying Yang, Xiuping Li, Shikun Ma and Lei Zhang for administrative assistance, to Wang Kang (BIG, CAS) for his help in RNA-seq analysis, to Wei Li, Jingyi Jia (Xuanwu Hospital Capital Medical University) and Lukai Huang (IOZ, CAS) for their help in the management of laboratory animals, and to Xixia Li and Xueke Tan (IBP, CAS) for their help in transmission electron microscopy. This work was supported by the National Key Research and Development Program of China (2018YFA0107203), the Strategic Priority Research Program of the Chinese Academy of Sciences (XDA16010000), the National Key Research and Development Program of China (2020YFA0804000, 2018YFC2000100, 2020YFA0112201, 2017YFA0103304, 2017YFA0102802, 2020YFA0113400, 2019YFA0110100), the National Natural Science Foundation of China (Grant Nos. 81901433, 81921006, 81625009, 91749202, 81861168034, 91949209, 92049304, 81822018, 92049116, 82071588, 32000500, 81922027, 81870228, 82125011, 82122024, 32100937, 92149301, 92168201), the Key Research Program of the Chinese Academy of Sciences (KFZD-SW-221), the Program of Beijing Municipal Science and Technology Commission (Z191100001519005), the Program of the Beijing Natural Science Foundation (Z190019, JQ20031), K. C. Wong Education Foundation (GJTD-2019-06, GJTD-2019-08), Beijing Hospitals Authority Youth Programme (QML20200802), Youth Innovation Promotion Association of CAS (2021078, E1CAZW0401), the 14th Five-year Network Security and Informatization Plan of Chinese Academy of Sciences (WX145XQ07-18), the Non-profit Central Research Institute Fund of Chinese Academy of Medical Sciences (2020-JKCS-011), the State Key Laboratory of Stem Cell and Reproductive Biology, the State Key Laboratory of Membrane Biology, and the Milky Way Research Foundation (MWRF).

Qun Chu, Feifei Liu, Yifang He, Xiaoyu Jiang, Yusheng Cai, Zeming Wu, Kaowen Yan, Lingling Geng, Yichen Zhang, Huyi Feng, Kaixin Zhou, Si Wang, Weiqi Zhang, Guang-Hui Liu, Shuai Ma, Jing Qu and Moshi Song declared no conflict of interest. All institutional and national guidelines for the care and use of laboratory animals were followed.

Qun Chu[1,3,4,11], Feifei Liu[2,3,4], Yifang He[2,3,4,8], Xiaoyu Jiang[2,3,4,8], Yusheng Cai[2,3,4], Zeming Wu[2,3,4], Kaowen Yan[2,3,4], Lingling Geng[5,9], Yichen Zhang[2,3,4,8], Huyi Feng[11], Kaixin Zhou[12], Si Wang[5,9], Weiqi Zhang[3,5,6,7,8,9,10], Guang-Hui Liu[2,3,4,5,8,9]✉, Shuai Ma[2,3,4]✉, Jing Qu[1,3,4,8]✉, Moshi Song[2,3,4,8]✉

[1] State Key Laboratory of Stem Cell and Reproductive Biology, Institute of Zoology, Chinese Academy of Sciences, Beijing 100101, China
[2] State Key Laboratory of Membrane Biology, Institute of Zoology, Chinese Academy of Sciences, Beijing 100101, China
[3] Institute for Stem Cell and Regeneration, Chinese Academy of Sciences, Beijing 100101, China

[4] Beijing Institute for Stem Cell and Regenerative Medicine, Beijing 100101, China
[5] Advanced Innovation Center for Human Brain Protection, National Clinical Research Center for Geriatric Disorders, Xuanwu Hospital Capital Medical University, Beijing 100053, China
[6] CAS Key Laboratory of Genomic and Precision Medicine, Beijing Institute of Genomics, Chinese Academy of Sciences, Beijing 100101, China
[7] China National Center for Bioinformation, Beijing 100101, China
[8] University of Chinese Academy of Sciences, Beijing 100049, China
[9] Aging Translational Medicine Center, International Center for Aging and Cancer, Xuanwu Hospital, Capital Medical University, Beijing 100053, China
[10] Sino-Danish College, University of Chinese Academy of Sciences, Beijing 101408, China
[11] Chongqing Renji Hospital, University of Chinese Academy of Sciences, Chongqing 400062, China
[12] College of Life Sciences, University of Chinese Academy of Sciences, Beijing 100049, China
✉ Correspondence: ghliu@ioz.ac.cn (G.-H. Liu), mashuai@ioz.ac.cn (S. Ma), qujing@ioz.ac.cn (J. Qu), songmoshi@ioz.ac.cn (M. Song)

Accepted October 17, 2021

OPEN ACCESS

REFERENCES

Bantug GR, Fischer M, Grahlert J, Balmer ML, Unterstab G, Develioglu L, Steiner R, Zhang L, Costa ASH, Gubser PM et al (2018) Mitochondria-endoplasmic reticulum contact sites function as immunometabolic hubs that orchestrate the rapid recall response of memory CD8(+) T cells. Immunity 48:542-555.e6

Bi S, Liu Z, Wu Z, Wang Z, Liu X, Wang S, Ren J, Yao Y, Zhang W, Song M et al (2020) SIRT7 antagonizes human stem cell aging as a heterochromatin stabilizer. Protein Cell 11:483–504

de Jesus Domingues AM, Artegiani B, Dahl A, Calegari F (2016) Identification of Tox chromatin binding properties and downstream targets by DamID-Seq. Genom Data 7:264–268

Garcia-Prat L, Sousa-Victor P, Munoz-Canoves P (2017) Proteostatic and metabolic control of stemness. Cell Stem Cell 20:593–608

Gu W, Gaeta X, Sahakyan A, Chan AB, Hong CS, Kim R, Braas D, Plath K, Lowry WE, Christofk HR (2016) Glycolytic metabolism plays a functional role in regulating human pluripotent stem cell state. Cell Stem Cell 19:476–490

Hu J, Sun F, Chen W, Zhang J, Zhang T, Qi M, Feng T, Liu H, Li X, Xing Y et al (2019) BTF3 sustains cancer stem-like phenotype of prostate cancer via stabilization of BMI1. J Exp Clin Cancer Res 38:227

Mandal S, Lindgren AG, Srivastava AS, Clark AT, Banerjee U (2011) Mitochondrial function controls proliferation and early differentiation potential of embryonic stem cells. Stem Cells 29:486–495

Meng D, Frank AR, Jewell JL (2018) mTOR signaling in stem and progenitor cells. Development 145(1):dev152595

Schreiber KH, Arriola Apelo SI, Yu D, Brinkman JA, Velarde MC, Syed FA, Liao CY, Baar EL, Carbajal KA, Sherman DS et al (2019) A novel rapamycin analog is highly selective for mTORC1 in vivo. Nat Commun 10:3194

Shan H, Geng L, Jiang X, Song M, Wang J, Liu Z, Zhuo X, Wu Z, Hu J, Ji Z et al (2021) Large-scale chemical screen identifies gallic acid as a geroprotector for human stem cells. Protein Cell. https://doi.org/10.1007/s13238-021-00872-5

Wang JD, Shao Y, Liu D, Liu NY, Zhu DY (2021a) Rictor/mTORC2 involves mitochondrial function in ES cells derived cardiomyocytes via mitochondrial Connexin 43. Acta Pharmacol Sin. https://doi.org/10.1038/s41401-020-00591-3

Wang S, Cheng F, Ji Q, Song M, Wu Z, Zhang Y, Ji Z, Feng H, Belmonte JCI, Zhou Q et al (2021b) Hyperthermia differentially affects specific human stem cells and their differentiated derivatives. Protein Cell. https://doi.org/10.1007/s13238-021-00887-y

Wang S, Min Z, Ji Q, Geng L, Su Y, Liu Z, Hu H, Wang L, Zhang W, Suzuiki K et al (2020) Rescue of premature aging defects in Cockayne syndrome stem cells by CRISPR/Cas9-mediated gene correction. Protein Cell 11:1–22

Zheng B, Wang J, Tang L, Tan C, Zhao Z, Xiao Y, Ge R, Zhu D (2017) Involvement of Rictor/mTORC2 in cardiomyocyte differentiation of mouse embryonic stem cells in vitro. Int J Biol Sci 13:110–121

Zhu Y, Wang P, Zhang L, Bai G, Yang C, Wang Y, He J, Zhang Z, Zhu G, Zou D (2019) Superhero Rictor promotes cellular differentiation of mouse embryonic stem cells. Cell Death Differ 26:958–968

Qun Chu, Feifei Liu, Yifang He, and Xiaoyu Jiang contributed equally.

Supplementary Information The online version contains supplementary material available at https://doi.org/10.1007/s13238-021-00898-9.

Supplemental Materials

Materials and Methods

Cell culture

RICTOR$^{+/+}$ and *RICTOR*$^{-/-}$ hESCs were cultured on feeder cells (mouse embryonic fibroblasts, MEFs) in hESC medium with DMEM/F12 (Invitrogen) supplemented with 20% Knockout Serum Replacement (Invitrogen), 2 mM GlutaMAX (Invitrogen), 0.1 mM non-essential amino acids (NEAA, Invitrogen), 1% penicillin/streptomycin (Invitrogen), 55 μM β-mercaptoethanol (Invitrogen), and 10 ng/mL FGF2 (Joint Protein Central) or on Matrigel (BD Biosciences) in mTeSR medium (STEMCELL Technology) in an incubator at 37℃ with 5% CO_2.

Generation of *RICTOR*-knockout (*RICTOR*$^{-/-}$) hESCs

CRISPR/Cas9-mediated gene knockout was performed as previously described with minor modifications (Cheng et al., 2019). Specifically, the guide RNA (gRNA) (5'-AATATGGCGGCGATCGGCCGCGG-3') targeting the exon 1 of the *RICTOR* gene was cloned into the pCAG-mCherry-sgRNA vector (Addgene, #87110). H9 ESCs were cultured on Matrigel-coated plates for 4-5 days and then treated with ROCK inhibitor (Selleck Y-27632) overnight. The following day, 5×10^6 single cells were obtained via trypsinization and mixed with 100 μL Opti-MEM containing 14 μg pCAG-Cas9-2AGFP vectors (Addgene #87109) and 7 μg pCAG-mCherry-Rictor-gRNA vectors before the electroporation. After the electroporation, the cells were seeded on Matrigel-coated plates with mTeSR medium containing ROCK inhibitor. After 48 hr, cells were digested into single cells, and purified by fluorescence activated cell sorting (FACS) to obtain GFP and mCherry double-positive cells. Purified cells were seeded and cultured on MEF-coated plates. Clones were finally collected after about 10 days and subjected to the verification of gene editing success as well as downstream analyses.

Generation and characterization of hMSCs

Differentiation of hESCs into hMSCs was described previously (Zhang et al., 2019). Briefly, embryoid bodies (EBs) were formed from hESC clones in an ultralow attachment 6-well plate (Corning) in low-FGF2 hESC medium and were transferred to a Matrigel-coated plate in hMSC differentiation medium (hMSC culture medium supplemented with additional 9 ng/mL FGF2 and 5 ng/mL TGFβ (HumanZyme)). After 7 to 10 days, the cells became confluent and were further maintained in hMSC culture medium. hMSCs with triple positivity for CD73, CD90

and CD105 were sorted by flow cytometry and subjected to downstream analyses. The following antibodies were used: CD73-PE (BD Biosciences, 550257), CD90-FITC (BD Biosciences, 555595) and CD105-APC (Biolegend, 800508). The differentiative abilities of hMSCs were tested by differentiation into osteoblasts, chondrocytes and adipocytes as previously described (Zhang et al., 2019) and assessment with von Kossa staining (osteogenesis), toluidine blue staining (chondrogenesis) and Oil red O staining (adipogenesis), respectively.

Generation and characterization of hNSCs

hNSC differentiation from hESCs was conducted as previously described (Cheng et al., 2019). Briefly, hESCs were cultured on MEF feeders in neural induction medium-1 (neural stem cell maintenance medium supplemented with 1 μM CHIR99021, 1 μM SB431542, 2 μM dorsomorphin (Sigma) and 0.1 μM Compound E (EMD Chemicals Inc.) for two days, followed by neural induction medium-2 (neural induction medium-1 without dorsomorphin) for five days. The cells were subsequently cultured in Matrigel-coated plates in neural stem cell maintenance medium.

Neuronal differentiation from hNSCs

hNSCs were plated at a density of 3×10^4 cells per well in Matrigel-coated 24-well plates and cultured in neural stem cell maintenance medium for one to three days. The cells were then cultured in neuronal differentiation medium containing DMEM/F12, 1× N2, 1× B27, 200 μM Ascorbic acid (Sigma), 400 μM dbcAMP (Sigma), 10 ng/mL GDNF (Peprotech) and 10 ng/mL of BDNF (Peprotech) for two days before 20 μg/mL laminin (Sigma) was added to promote further differentiation.

Quantification of mRNA using real-time RT-PCR

Total RNAs were extracted from the cells with TRIzol Reagent (Thermo Fisher Scientific). Next, 2 μg of total RNA per sample was used for cDNA synthesis with the GoScript Reverse Transcription System (Promega) following the manufacturer's instruction. RT-qPCR was performed on a QuantStudio™ 5 Real-Time PCR System (Applied Biosystems) using THUNDERBIRD SYBR qPCR Mix (TOYOBO). The relative expression of each gene was normalized to the GAPDH transcript. The primer sequences are listed in Supplementary Table S1.

Western blot analysis

The cells were lysed in RIPA buffer (Beyotime, P0013B) supplemented with a protease inhibitor cocktail (Roche, 4693159001) and a phosphatase inhibitor (Roche, 4906837001) and then centrifuged at 14,000 *g* for 15 min at 4℃. The supernatants were collected and quantified using a BCA protein quantification kit (Beijing Dingguo Changsheng Biotechnology, BCA-02), heat-denatured in 1× SDS loading buffer (Beijing Dingguo Changsheng Biotechnology, WB-0091) at 105℃ for 5 min. The samples were then subjected to SDS-PAGE separation and electrotransferred onto 0.2 μm PVDF membrane (Millipore, ISEQ00010). The membrane was incubated with 5% (w/v) nonfat powdered milk (BBI Life Sciences, a600669-0250) for 1 hr at room temperature and then incubated with primary antibodies at 4℃ overnight. HRP-conjugated secondary antibodies were used for incubation at room temperature for 1 hr before the visualization by using a ChemiDoc XRS+ system (Bio-Rad) and the data were analyzed with ImageJ. The primary antibodies used were as follows: RICTOR (Cell Signaling Technology, 2114), OCT3/4 (Santa Cruz, sc-5279), SOX2 (Santa Cruz, sc-17320), NANOG (Abcam, ab21624), AKT (Cell Signaling Technology, 4691), phospho-AKT (Ser473) (Cell Signaling Technology, 4060), β-Tubulin (Immunoway, YM3030), GAPDH (Santa Cruz, sc-69879), HRP-conjugated goat anti-mouse IgG (Jackson ImmunoResearch Laboratories, 115-035-003) and HRP-conjugated goat anti-rabbit IgG (Jackson ImmunoResearch Laboratories, 111-035-003).

Immunofluorescence staining

Cells were fixed with 4% paraformaldehyde for 20 min, permeabilized in 0.4% Triton X-100 in PBS for 20 min and incubated with 10% donkey serum in PBS for 20 min at room temperature. The cells were then incubated with primary antibodies at 4℃ overnight followed by incubation with secondary antibodies as appropriate and Hoechst 33342 (Invitrogen) for 5 min at room temperature. The following antibodies were used: Ki67 (ZSGB-Bio, ZM-0166), PAX6 (Biolegend, 901301), SOX2 (Santa Cruz, sc17320), MAP2 (Sigma, M4403), β-tubulin III (TuJ1, Sigma, T2200), α-SMA (ZSGB-Bio, ZM-0003), FOXA2 (Cell Signaling Technology, 8186), Alexa 488 donkey anti-mouse IgG (Thermo Fisher Scientific, A21202), Alexa 568 donkey anti-rabbit IgG (Thermo Fisher Scientific, A10042) and Alexa 647 donkey anti-goat IgG (Thermo Fisher Scientific, A21447).

Alkaline phosphatase (AP) staining

An alkaline phosphatase detection kit (STEMGENT, 00-0055) was used for monitoring hESC undifferentiation through AP activity by immunocytochemistry staining. In brief, hESCs were fixed at room temperature for 3 min and washed with PBST (PBS containing 0.05% Tween-20). Fixed cells were then incubated in freshly prepared AP staining solution in the dark at room temperature for 15 min. The relative AP staining intensity was measured using ImageJ.

Teratoma formation assay

Teratoma formation assay was performed as previously described (Diao et al., 2021). In brief, 4×10^6 hESCs were collected and mixed with Matrigel:mTeSR (1: 4) solution. The mixture was then injected subcutaneously into the inguinal region of 6-week male NOD/SCID mice. The mice were monitored for teratoma formation and euthanized at about 10 weeks after the injection before the teratomas were collected for further analysis. The animal experiments performed in this study were approved by the Chinese Academy of Sciences Institutional Animal Care and Use Committee.

Clonal expansion assay

Briefly, 2×10^3 cells were seeded in 12-well plates and cultured for approximately 13 days. The cells were then fixed with 4% PFA for 30 min and stained with 0.2% crystal violet (Biohao, C0520) for 1 hr at room temperature and washed gently with running tap water. The relative cell density was measured using ImageJ.

Cell cycle analysis

For cell cycle analysis, 1×10^6 cells were collected and fixed in 75% ice-cold ethanol at -20℃ overnight. Then, cells were washed twice with PBS and stained with 0.02 mg/mL propidium iodide and 0.2 mg/mL RNase at 37℃ for 30 min. Cells were then analyzed by flow cytometry (BD LSR Fortessa).

Transmission electron microscopy

Transmission electron microscopy was performed to observe mitochondrial ultrastructure as previously reported (Diao et al., 2021). In brief, the cells were seeded onto Matrigel-coated microscope coverslips and fixed with 2.5% (vol/vol) glutaraldehyde at 4℃. The samples were dehydrated with graded alcohol and embedded in SPI-PON812 resin. Ultrathin sections with 70-nm thickness were obtained and then double-stained with uranyl acetate and lead citrate. Spirit Transmission Electron Microscope (FEI Company) was used to observe ultrastructure.

Mitochondrial numbers per cell were analyzed using ImageJ.

Measurement of mitochondrial mass, reactive oxygen species (ROS) and membrane potential

For mitochondrial mass measurement, cells were incubated with 10 μM of nonyl acridine orange (NAO, Thermo Fisher Scientific, A1372) for 10 min at 37℃ and then measured by flow cytometry (BD LSRFortessa). For mitochondrial ROS level determination, cells were stained with MitoSOX Red (Thermo Fisher Scientific, M36008) for about 20 min at 37℃ in the dark, and then analyzed by flow cytometry (BD LSRFortessa). For the assessment of mitochondrial membrane potential, cells were incubated with 1× JC-10 dye-loading solution (AAT Bioquest, 22801) at 37℃ for 30 min, then measured by flow cytometry (BD LSRFortessa) and analyzed using FlowJo software. The ratio of fluorescence intensities Ex/Em = 490/590 (JC-10 aggregate emission) and 490/530 nm (JC-10 monomer emission) (FL590/FL530) were calculated to define mitochondrial membrane potentials.

Seahorse XF analysis

Cells were seeded onto a 96-well Seahorse XF96 extracellular analyzer plate at a density of 4×10^4 cells per well for hESCs, 3×10^4 cells per well for hMSCs and 4×10^4 cells per well for hNSCs. One day prior to the experiment, calibrant solution was added to XFe96 sensor cartridges and incubated overnight under 37℃ without CO_2. On the day of the experiment, cells were washed twice and incubated for 45 min at 37℃ with Seahorse assay media containing 10 mM Glucose, 1 mM sodium pyruvate and 2 mM L-Glutamine for mitochondrial stress protocol and 2 mM L-Glutamine only for glycolysis stress protocol. After 15 min of equilibration, for oxygen consumption rate (OCR) measurement, oligomycin, FCCP and rotenone/antimycin A were loaded into ports of the XF cartridge to achieve final concentrations of 1.5 μM, 1 μM and 0.5 μM in the reaction, respectively. For extracellular acidification rate (ECAR) analysis, glucose, oligomycin, 2-DG were loaded into ports of the XF cartridge to achieve final concentrations of 10 mM, 1 μM and 50 mM in the reaction, respectively. After the analysis, cells were fixed in 4% formaldehyde for 30 min and then incubated with Hoechst 33342 for 15 min at room temperature to perform nuclei count for data normalization for each well.

RNA-seq library construction and sequencing

Briefly, total RNAs were extracted using TRIzol Reagent and genomic DNA was removed

using a DNA-free Kit. Library preparation was achieved by using a NEBNext® UltraTM Directional RNA Library Prep Kit for Illumina (New England Biolabs). Quality control and sequencing on Illumina HiSeq X Ten platforms were performed by Novogene Bioinformatics Technology Co., Ltd.

RNA-seq data processing

For RNA-seq data, Trim Galore (version 0.5.0) was used to trim and filter reads. The filtered data were mapped to the UCSC human hg19 genome using HISAT2 (version 2.0.4) (Kim et al., 2015). Then, the mapped data for each gene were counted using HTSeq (version 0.11.0) (Anders et al., 2015). Differentially expressed genes (DEGs) were identified using the DESeq2 (version 1.26.0) (Love et al., 2014) with the cutoff Benjamini-Hochberg adjusted *P* value of 0.05 and the absolute fold change more than $\log_2(1.5)$. Enrichment analysis was performed using Metascape (http://metascape.org/gp/) (Zhou et al., 2019). The DEGs are listed in Supplementary Table S2.

CNV analysis

Raw data were trimmed using Trim Galore software. Trimmed data were mapped to the human reference genome (hg19) using Bowtie2 (version 2.2.9) (Langmead and Salzberg, 2012). Then, duplicate reads were removed using Picard (http://broadinstitute.github.io/picard) software. ReadCounter was used to calculate reads number for each 0.5 Mb and the R package HMMcopy (version 1.28.1) (Ha et al., 2012) was used to calculate CNVs.

Statistical analysis

Data are presented as the mean ± SEM. GraphPad Prism software was used to perform a two-tailed Student's *t*-test. Statistical significance was presented as $*P < 0.05$, $**P < 0.01$ and $***P < 0.001$.

Data availability

Whole genome sequencing and RNA-seq data generated in this study have been deposited in the Genome Sequence Archive in the National Genomics Data Center, Beijing Institute of Genomics (China National Center for Bioinformation) of the Chinese Academy of Sciences, under accession number HRA001236 that are publicly accessible at http://bigd.big.ac.cn/gsa-human. These data can also be accessed via an interactive user-friendly webtool at Aging Atlas (https://bigd.big.ac.cn/aging/index) (Aging Atlas Consortium, 2021).

References

Aging Atlas Consortium. (2021). Aging Atlas: a multi-omics database for aging biology. Nucleicacids research 49, D825-D830.

Anders, S., Pyl, P.T., and Huber, W. (2015). HTSeq--a Python framework to work with high-throughput sequencing data. Bioinformatics 31, 166-169.

Cheng, F., Wang, S., Song, M., Liu, Z., Liu, P., Wang, L., Wang, Y., Zhao, Q., Yan, K., Chan, P.*, et al.* (2019). DJ-1 is dispensable for human stem cell homeostasis. Protein Cell 10, 846-853.

Diao, Z., Ji, Q., Wu, Z., Zhang, W., Cai, Y., Wang, Z., Hu, J., Liu, Z., Wang, Q., Bi, S.*, et al.* (2021). SIRT3 consolidates heterochromatin and counteracts senescence. Nucleic Acids Res 49, 4203-4219.

Ha, G., Roth, A., Lai, D., Bashashati, A., Ding, J., Goya, R., Giuliany, R., Rosner, J., Oloumi, A., Shumansky, K.*, et al.* (2012). Integrative analysis of genome-wide loss of heterozygosity and monoallelic expression at nucleotide resolution reveals disrupted pathways in triple-negative breast cancer. Genome Res 22, 1995-2007.

Kim, D., Langmead, B., and Salzberg, S.L. (2015). HISAT: a fast spliced aligner with low memory requirements. Nat Methods 12, 357-360.

Langmead, B., and Salzberg, S.L. (2012). Fast gapped-read alignment with Bowtie 2. Nat Methods 9, 357-359.

Love, M.I., Huber, W., and Anders, S. (2014). Moderated estimation of fold change and dispersion for RNA-seq data with DESeq2. Genome Biol 15, 550.

Zhang, X., Liu, Z., Liu, X., Wang, S., Zhang, Y., He, X., Sun, S., Ma, S., Shyh-Chang, N., Liu, F.*, et al.* (2019). Telomere-dependent and telomere-independent roles of RAP1 in regulating human stem cell homeostasis. Protein Cell 10, 649-667.

Zhou, Y., Zhou, B., Pache, L., Chang, M., Khodabakhshi, A.H., Tanaseichuk, O., Benner, C., and Chanda, S.K. (2019). Metascape provides a biologist-oriented resource for the analysis of systems-level datasets. Nat Commun 10, 1523.

Figure S1

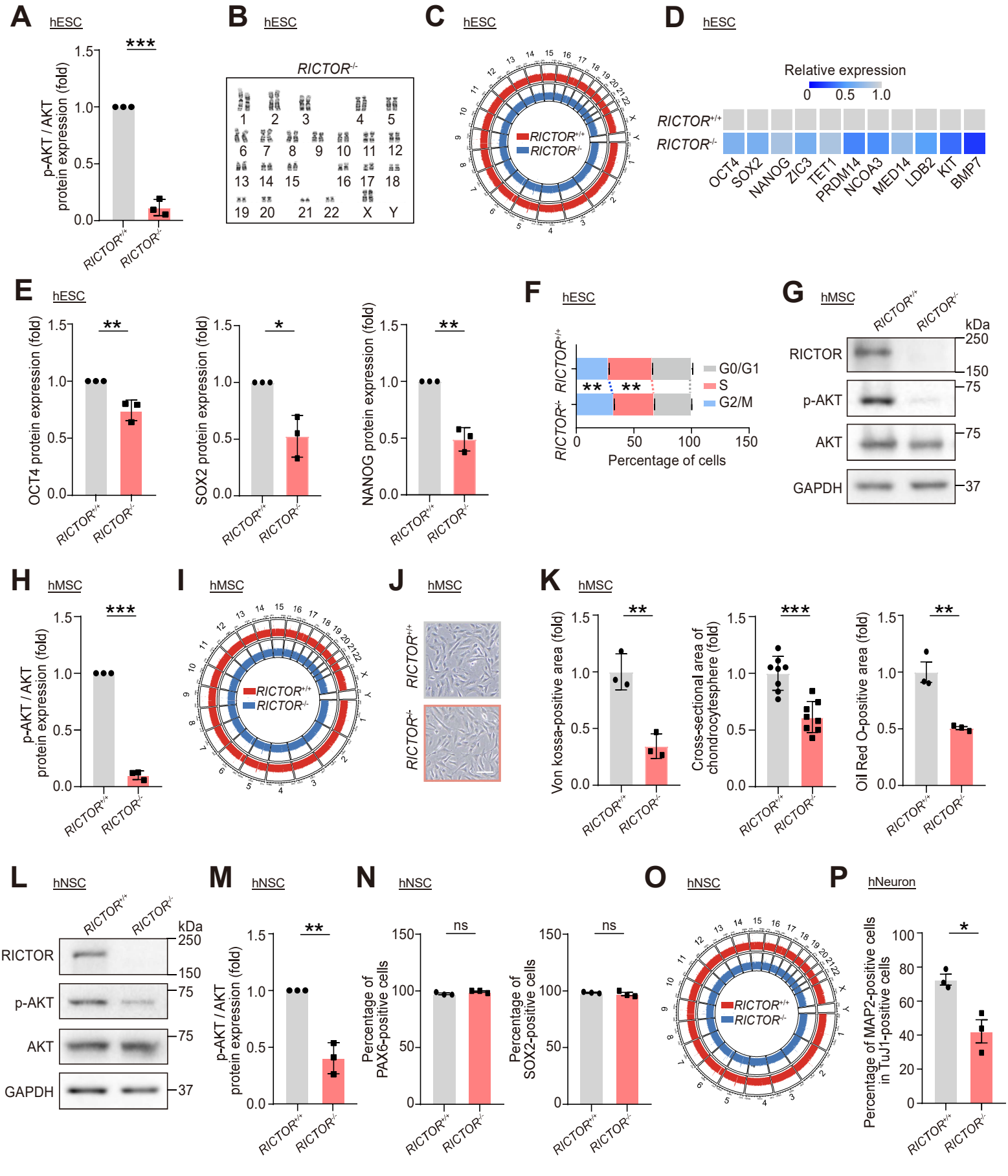
A hESC
p-AKT / AKT protein expression (fold)
RICTOR+/+
RICTOR-/-
B hESC
RICTOR-/-
C hESC
D hESC
Relative expression
OCT4
SOX2
NANOG
ZIC3
TET1
PRDM14
NCOA3
MED14
LDB2
KIT
BMP7
E hESC
OCT4 protein expression (fold)
SOX2 protein expression (fold)
NANOG protein expression (fold)
F hESC
G0/G1
S
G2/M
Percentage of cells
G hMSC
kDa
RICTOR
p-AKT
AKT
GAPDH
H hMSC
I hMSC
J hMSC
K hMSC
Von kossa-positive area (fold)
Cross-sectional area of chondrocytesphere (fold)
Oil Red O-positive area (fold)
L hNSC
M hNSC
N hNSC
Percentage of PAX6-positive cells
ns
O hNSC
Percentage of SOX2-positive cells
P hNeuron
Percentage of MAP2-positive cells in TuJ1-positive cells

Figure S2

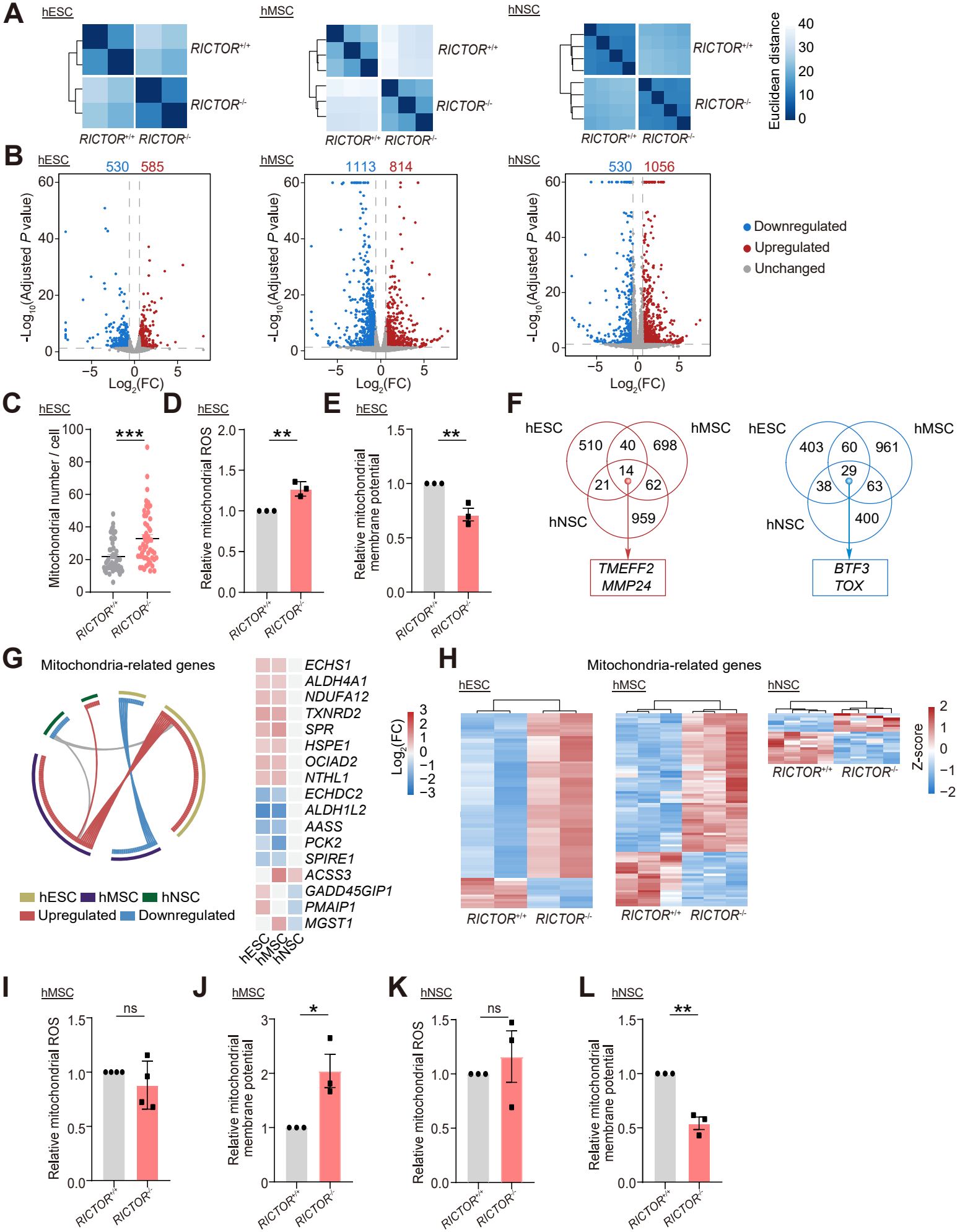
A
hESC
hMSC
hNSC
RICTOR+/+
RICTOR-/-
Euclidean distance
40
30
20
10
0
B
hESC
530 585
hMSC
1113 814
hNSC
530 1056
-Log10(Adjusted P value)
Log2(FC)
Downregulated
Upregulated
Unchanged
C
hESC
Mitochondrial number / cell
***
D
hESC
Relative mitochondrial ROS
**
E
hESC
Relative mitochondrial membrane potential
**
F
hESC
hMSC
hNSC
510
40
698
14
21
62
959
TMEFF2
MMP24
403
60
961
29
38
63
400
BTF3
TOX
G
Mitochondria-related genes
hESC hMSC hNSC
Upregulated Downregulated
ECHS1
ALDH4A1
NDUFA12
TXNRD2
SPR
HSPE1
OCIAD2
NTHL1
ECHDC2
ALDH1L2
AASS
PCK2
SPIRE1
ACSS3
GADD45GIP1
PMAIP1
MGST1
H
Mitochondria-related genes
Log2(FC)
Z-score
I
hMSC
ns
Relative mitochondrial ROS
J
hMSC
*
Relative mitochondrial membrane potential
K
hNSC
ns
Relative mitochondrial ROS
L
hNSC
**
Relative mitochondrial membrane potential

Supplemental Figure Legends

Figure S1. Phase-contrast images, quantifications of multiple RNAs and proteins, and functional analyses of RICTOR-deficient hESCs, hMSCs and hNSCs.

(A) Quantification of normalized phosphorylated AKT Ser473 levels to total AKT expression in *RICTOR*$^{+/+}$ and *RICTOR*$^{-/-}$ hESCs. Data are presented as mean ± SEM of three independent experiments. ***$P < 0.001$. These quantitative results are related to Fig 1C. **(B)** Karyotype analysis of *RICTOR*$^{-/-}$ hESCs. **(C)** Genome-wide analysis of copy number variations (CNVs) by whole genome sequencing in *RICTOR*$^{+/+}$ and *RICTOR*$^{-/-}$ hESCs. **(D)** Heatmap showing the mRNA expression of the pluripotency markers *OCT4*, *SOX2*, *NANOG* and a few other genes related to stem cell population maintenance in *RICTOR*$^{+/+}$ and *RICTOR*$^{-/-}$ hESCs. **(E)** Western blot analysis of protein expression of hESC pluripotency markers OCT4, SOX2 and NANOG in *RICTOR*$^{+/+}$ and *RICTOR*$^{-/-}$ hESCs. β-tubulin was used as the loading control. Data are presented as mean ± SEM of three independent experiments. **$P < 0.01$, *$P < 0.05$. These quantitative results are related to Fig 1E. **(F)** Cell cycle analysis of *RICTOR*$^{+/+}$ and *RICTOR*$^{-/-}$ hESCs. Data are presented as mean ± SEM of three biological repeats. **$P < 0.01$. **(G)** Western blot analysis of RICTOR, phosphorylated AKT Ser473 level and total AKT expression in *RICTOR*$^{+/+}$ and *RICTOR*$^{-/-}$ hMSCs. GAPDH was used as the loading control. **(H)** Quantification of normalized phosphorylated AKT Ser473 levels to total AKT expression in *RICTOR*$^{+/+}$ and *RICTOR*$^{-/-}$ hMSCs. Data are presented as mean ± SEM of three independent experiments. ***$P < 0.001$. **(I)** Genome-wide analysis of copy number variations (CNVs) by whole genome sequencing in *RICTOR*$^{+/+}$ and *RICTOR*$^{-/-}$ hMSCs. **(J)** Representative phase-contrast images of *RICTOR*$^{+/+}$ and *RICTOR*$^{-/-}$ hMSC colonies. Scale bar, 100 μm. **(K)** Quantifications of the multilineage differentiation potentials of hMSCs. Left, osteogenesis of *RICTOR*$^{+/+}$ and *RICTOR*$^{-/-}$ hMSCs evaluated by von Kossa staining. Data are presented as mean ± SEM of three biological repeats. **$P < 0.01$. Middle, chondrogenesis of *RICTOR*$^{+/+}$ and *RICTOR*$^{-/-}$ hMSCs evaluated by Toluidine blue staining. Data are presented as mean ± SEM of eight biological repeats. ***$P < 0.001$. Right, adipogenesis of *RICTOR*$^{+/+}$ and *RICTOR*$^{-/-}$ hMSCs evaluated by Oil Red O staining. Data are presented as mean ± SEM of three biological repeats. **$P < 0.01$. These quantitative results are related to Fig 1M. **(L)** Western blot analysis of RICTOR, phosphorylated AKT Ser473 level and total AKT expression in *RICTOR*$^{+/+}$ and

RICTOR$^{-/-}$ hNSCs. GAPDH was used as the loading control. **(M)** Quantification of normalized phosphorylated AKT Ser473 levels to total AKT expression in *RICTOR*$^{+/+}$ and *RICTOR*$^{-/-}$ hNSCs. Data are presented as mean ± SEM of three independent experiments. $^{**}P < 0.01$. **(N)** Quantifications of immunofluorescence staining for hNSC-specific markers PAX6 and SOX2 in *RICTOR*$^{+/+}$ and *RICTOR*$^{-/-}$ of hNSCs. Data are presented as mean ± SEM of three biological repeats. ns, not significant. These quantitative results are related to Fig 1N. **(O)** Genome-wide analysis of copy number variations (CNVs) by whole genome sequencing in *RICTOR*$^{+/+}$ and *RICTOR*$^{-/-}$ hNSCs. (P) Quantifications of the percentages of MAP2-positive cells in TuJ1-positive cells in *RICTOR*$^{+/+}$ and *RICTOR*$^{-/-}$ hNeurons. Data are presented as mean ± SEM of three biological repeats. $^{*}P < 0.05$. These quantitative results are related to Fig 1Q.

Figure S2. RNA sequencing analysis and functional analysis of RICTOR-deficient hESCs, hMSCs and hNSCs.

(A) Heatmap showing the Euclidean distance between RNA-seq replicates of *RICTOR*$^{+/+}$ and *RICTOR*$^{-/-}$ hESCs, hMSCs and hNSCs. **(B)** Volcano plot of differentially expressed genes in *RICTOR*$^{+/+}$ and *RICTOR*$^{-/-}$ hESCs, hMSCs and hNSCs. **(C)** Transmission electron microscopy analysis of mitochondrial number in *RICTOR*$^{+/+}$ and *RICTOR*$^{-/-}$ hESCs. Data are presented as mean ± SEM of 50 cells. $^{***}P < 0.001$. These quantitative results are related to Fig 2C. **(D)** Flow cytometric analysis of mitochondrial ROS in *RICTOR*$^{+/+}$ and *RICTOR*$^{-/-}$ hESCs. Data are presented as mean ± SEM of three independent experiments. $^{**}P < 0.01$. **(E)** Flow cytometric analysis of relative mitochondrial membrane potential in *RICTOR*$^{+/+}$ and *RICTOR*$^{-/-}$ hESCs. Data are presented as mean ± SEM of three independent experiments. $^{**}P < 0.01$. **(F)** Shared upregulated and downregulated genes in *RICTOR*$^{+/+}$ and *RICTOR*$^{-/-}$ hESCs, hMSCs and hNSCs. Red indicates upregulated gene and blue indicates downregulated gene. **(G)** Shared mitochondria-related genes in *RICTOR*$^{+/+}$ and *RICTOR*$^{-/-}$ hESCs, hMSCs and hNSCs. **(H)** Heatmaps showing the expression levels of mitochondria-related genes in *RICTOR*$^{+/+}$ and *RICTOR*$^{-/-}$ hESCs, hMSCs and hNSCs. **(I)** Flow cytometric analysis of mitochondrial ROS in *RICTOR*$^{+/+}$ and *RICTOR*$^{-/-}$ hMSCs. Data are presented as mean ± SEM of four independent experiments. ns, not significant. **(J)** Flow cytometric analysis of relative mitochondrial membrane potential in *RICTOR*$^{+/+}$ and *RICTOR*$^{-/-}$ hMSCs. Data are presented as mean ± SEM

of three independent experiments. *$P < 0.05$. **(K)** Flow cytometric analysis of mitochondrial ROS in *RICTOR*$^{+/+}$ and *RICTOR*$^{-/-}$ hNSCs. Data are presented as mean ± SEM of three independent experiments. ns, not significant. **(L)** Flow cytometric analysis of relative mitochondrial membrane potential in *RICTOR*$^{+/+}$ and *RICTOR*$^{-/-}$ hNSCs. Data are presented as mean ± SEM of three independent experiments. **$P < 0.01$.

Supplemental Table Legends

Table S1. RNA primers for qRT-PCR assay.

Table S2. DEGs in *RICTOR*$^{-/-}$ versus *RICTOR*$^{+/+}$ hESCs, hMSCs and hNSCs.